

LIGO core-collapse supernova detection using convolution neural networks

Zhicheng Pan,¹* El Mehdi Zahraoui,²† Guillermo Cabrera-Guerrero³‡ and Patricio Maturana-Russel^{2,4}§

¹Electrical Engineering Department, Auckland University of Technology, Auckland, New Zealand

²Mathematical Sciences Department, Auckland University of Technology, Auckland, New Zealand

³School of Computer Engineering, Pontificia Universidad Católica de Valparaíso, Valparaíso, Chile

⁴Department of Statistics, University of Auckland, Auckland, New Zealand

Accepted XXX. Received YYY; in original form ZZZ

ABSTRACT

Core-Collapse Supernovae (CCSNe) remain a critical focus in the search for gravitational waves (GWs) in modern astronomy. Their detection and subsequent analysis will enhance our understanding of the explosion mechanisms in massive stars. This paper investigates a combination of time-frequency analysis tools with convolutional neural network (CNN) to enhance the detection of GWs originating from CCSNe. The CNN was trained on simulated CCSNe signals and Advanced LIGO (aLIGO) noise in two instances, using spectrograms computed from two time-frequency transformations: the short-time Fourier transform (STFT) and the Q-transform. The algorithm detects CCSNe signals based on their time-frequency spectrograms. Our CNN model achieves a near 100% true positive rate for CCSNe GW events with a signal-to-noise ratio (SNR) greater than 0.5 in our test set. We also found that the STFT outperforms the Q-transform for SNRs below 0.5.

Key words: Core-collapse supernovae; CNN; Q-transform; aLIGO.

1 INTRODUCTION

Since Sir Isaac Newton, the nature of gravity has become one of the main subjects in physics. Newton initially described gravity as a force of attraction between masses in the 17th century. Newton’s law of universal gravitation revolutionized our understanding of celestial mechanics, explaining the motion of the moon and planets. However, the Newtonian framework had limitations, especially in explaining phenomena at cosmic scales. In the 20th century, Albert Einstein shifted our understanding of the nature of gravity by formulating the General Theory of Relativity (Einstein et al. 1916). This theory re-defined gravity not as a force but rather as a mass curving spacetime, with spacetime dictating the movement of the mass. General relativity predicted phenomena that Newtonian physics could not account for, such as the bending of light by gravity, and described astrophysical dynamics precisely, such as the precession of planetary orbits. Einstein’s theory also led to the prediction of gravitational waves (GWs) that required a century of technological revolutions to validate empirically. GWs are ripples in spacetime that emerge from the universe’s most violent and energetic processes, such as the mergers of black holes and neutron stars (Abbott et al. 2017a). GWs carry information about their origins and the nature of gravity, providing a novel method for observing and understanding the universe.

The first GW detection, resulting from the merger of a pair of black

holes with masses of approximately 36 and 29 solar masses, was announced on February 11, 2016 (Abbott et al. 2016a). The event was observed on the 14th of September 2015 by the Advanced Laser Interferometer Gravitational-Wave Observatory (aLIGO)’s Livingston and Hanford observatories, validating a crucial prediction of Einstein’s general relativity theory and offering the inaugural direct proof of black hole mergers. LIGO detectors are GW interferometers based on Michelson’s interferometer experiment. The LIGO interferometer is an optical instrument that splits a laser beam into two perpendicular arms and uses mirrors to reflect the laser beams to the photodetectors (see Figure 1). The interference between the two laser beams will occur if the length of one of the arms or both changes, which will induce a phase shift in the laser beams. This phase shift is used to detect the changes in distance. LIGO has approximately 4 km long arms with a sensitivity of GW characteristic strain up to about 10^{-23} . The ground-based interferometer can detect GWs in the 200 Hz – 10 kHz frequency range (Aasi et al. 2015). Detection of GWs in a lower frequency range will be possible through LISA, a space-based interferometer built to observe in the μ Hz-Hz frequency range (Danzmann & Rüdiger 2003). LISA is scheduled to launch by 2034. For even lower frequencies, the Pulsar Timing Array (PTA) extends the sensitivity to the nHz- μ Hz range, helping to understand the early dynamics of astrophysical events (Agazie et al. 2023).

aLIGO has been successful over the last decade in detecting and probing the GWs of multiple astrophysical phenomena (Abbott et al. 2016b, 2017b). However, despite being one of the main targets of these interferometers, the GW signals from Core-Collapse Supernovae (CCSNe) have yet to be detected. A Core-Collapse supernova is a powerful and catastrophic stellar explosion that occurs at the

* E-mail: steven.pan@autuni.ac.nz

† E-mail: elmehdi.zahraoui@autuni.ac.nz

‡ E-mail: guillermo.cabrera@pucv.cl

§ E-mail: p.maturana.russel@aut.ac.nz

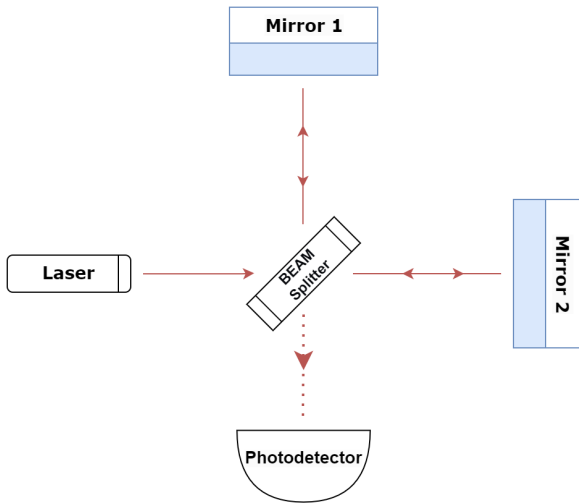


Figure 1. A simplified LIGO diagram with two perpendicular interferometry arms.

end of a massive star’s life cycle, when the core of the star, typically composed of iron, collapses under its gravity, emitting high luminosity light. Its luminosity can be brighter than the moon’s brightness and can last for a few weeks before fading away. This phenomenon is considered among the most powerful explosions in the universe, releasing 10^{53} erg of gravitational binding energy. Although CCSNe have been detected and studied across the electro-magnetic (EM) spectrum, they cannot uncover the processes deep in the star’s core when the explosion ignites (Vink 2020). Therefore, studying CCSNe through GW spectrum will unveil the processes contributing to this stellar explosion. In this article, we will focus on detecting GWs emerging from CCSNe.

The current understanding of CCSNe dynamics is based on two models: the neutrino-driven mechanism and the magneto-rotational mechanism. A multi-messenger study of CCSNe by combining GW and EM spectra will help settle and evaluate our understanding of the two current models used for simulating GWs from CCSNe. The two models are currently used in two-dimensional (Bizouard et al. 2021) and three-dimensional (Vartanyan et al. 2023) cases to simulate the interaction between particles and generate the signatures of GWs. These simulations are computationally expensive and require multiple iterations to initiate a supernova explosion (Müller et al. 2013). A portion of these simulations fail to achieve an explosion state, resulting in no generation of the CCSNe GWs (Bizouard et al. 2021). In Wolfe et al. (2023), a 28.3% (out of 1,684 simulations) failed to explode and no signature was obtained. This is due to many challenges facing the CCSNe simulation, where the resolution of the particles is the key to a successful simulation. The resolution of particles will determine how challenging the other constraints of this simulation are, such as the interactions of the electron, muon, tau neutrinos, and their anti-particles with ordinary matter (Astone et al. 2018). The resolution used to simulate these interactions also increases the complexity of the simulation, which needs to account for the relativistic effect, sophisticated equation of state, and more constraints to achieve realistic circumstances. Generating a bank of CCSNe waveforms is currently limited given the resources and computational power, which limits the number of GW templates to cover the parameter space of possible CCSNe events (Wolfe et al. 2023). The limitation of template-based matching, i.e., Coherent WaveBurst (cWB) pipeline proposed in Klimentenko et al. (2008), has prompted the exploration of alternative methods to the template-based ones.

Eventually, the new alternative methods may achieve the detection of the first CCSNe GW signal in the next decade.

Computer science has enabled the development and implementation of machine learning (ML) algorithms, i.e., algorithms that can learn from datasets and make predictions without being explicitly programmed. These algorithms became popular nowadays in signal and noise processing (Krishna et al. 2023). Recently, a few ML techniques, particularly convolutional neural networks (CNNs), have been proposed and successfully tested on simulated data for the detection of CCSNe signals (Astone et al. 2018; Chan et al. 2016). These results confirm that employing ML can significantly improve the detection sensitivity of gravitational wave signals by reducing false positives and filtering out noise events. In this article, we train two CNNs separately using time-frequency spectrograms from the short-time Fourier transform (STFT) and the Q-transform (QT) (Chatterji et al. 2004), computed from CCSNe GW signals and aLIGO noise data. While QT has been successfully utilized for parameter inference in gravitational wave data analysis, its application for detecting CCSNe signals represents a novel approach. We will compare the effectiveness of these two methodologies using datasets that include various equation of states (EOSs) and distances ranging from 0.1 to 10 kpc.

This paper is structured as follows. In Section 2, we review the work done on the detection of CCSNe and discuss recent alternatives with potential in this context. In Section 3, we describe how the simulated data is generated and our method for processing the data and detecting CCSNe. We present and discuss the results in Section 4. Finally, we conclude by summarizing the results, discussing the limitations of the proposed methodologies, and outlining future work.

2 LITERATURE REVIEW

Since their appearance, ML techniques have shown their ability to enhance and bypass many difficulties in problem-solving, especially in signal processing. Many studies have demonstrated the possibility of training a CNN on time series and spectrograms to classify signals, e.g., Krishna et al. (2023). GW astronomy has also incorporated machine learning techniques to enhance signal detection, especially for complex cases like searching for core-collapse supernovae signatures. Astone et al. (2018) made the first steps in CCSNe detection by taking advantage of the peculiarities of these GW signals, particularly the monotonic rise in frequency related to g-mode excitation. In their study, the simulated g-mode signature was injected into Gaussian noise to imitate the spectral behavior of LIGO. Then, the cWB pipeline was used to generate a time-frequency spectrogram, and a CNN was trained to classify these images of spectrograms into noise and noise + signal classes. This method offers a novel way to detect GWs from non-rotating or slowly rotating progenitor stars, expanding the scope of detectable GW events. On the other hand, Chan et al. (2016) explored the use of CNNs for the classification of GW signals from CCSNe. The CNN was tailored for multi-class classification, distinguishing between background noise and signals from different types of supernovae explosions magneto-rotational or neutrino-driven embedded in background noise. Additionally to aLIGO data, the CNN was trained with AdVirgo and KARGA, using a categorical cross-entropy loss function. The combination of four detectors allowed the authors to evaluate detections of potential extragalactic CCSNe GW events at 200 kpc. Antelis et al. (2022) marked a significant step forward in using supervised ML for GW detection from CCSNe. The cWB pipeline was integrated with ML classifiers like linear discriminant analysis (LDA) and support vec-

tor machines (SVM). The classifiers were trained on features of the reconstructed GW burst, such as duration, central frequency, and detection statistics provided by the cWB pipeline. The classification was done independently on each of the LIGO detectors. The CCSNe models considered distances ranging from 1 to 10 kpc. Recently, Nunes et al. (2024) tested deep learning techniques in the time domain and Neural Networks in the time–frequency domain to classify and infer on the CCSNe parameters. The study achieved better detection levels in the time domain, reaching 98% for signal-to-noise ratio (SNR) greater than 10. These studies have demonstrated the potential of machine learning techniques to unravel the complex nature of CCSNe and enhance the sensitivity and accuracy of GW detection.

The difficulty in detecting CCSNe signals lies, in part, in the need for robust signal extraction methods. Recent studies, such as Song et al. (2024a,b), have contributed significantly to developing adaptive neural control systems in noise reduction and signal tracking, laying foundational methods that can be extended to GW analysis. Similarly, Wang et al. (2023) proposed a reinforcement learning-based strategy, namely Q-Learning, for iterative optimization in complex system identification, offering a pathway for improving the detection pipeline for faint astrophysical signals. Recent advances in neural-network-based classification techniques (e.g., Abdullahi et al. (2024a,b)) present diverse opportunities for improving CCSNe detection, such as novel strategies for effective features selection, pooling strategies to avoid over-fitting, and the use of Fourier CNNs for pattern detection in real-time applications, among others. The literature on algorithms with potential for CCSNe detection is extensive but remains largely unexplored.

3 METHODS

First, we describe the CCSNe aLIGO (Aasi et al. 2015) data generation process in the time domain used in this study. Then, we discuss the pre-processing of the data before generating the spectrogram images using the popular STFT, one of the most frequently used tools in time-frequency analysis, and the QT, a very popular technique in aLIGO GW time-frequency data analysis. Finally, we describe the CNN proposed for CCSNe detection, including its architecture and the way it is trained, validated, and tested.

3.1 Data Generation

The positive class contains simulated CCSNe GW signals from eight EOS models: *s11.2*, *s15*, *s20*, *s25*, *s40* under *LS220*, *s15* under *GShen*, and *s15*, *s20* under *SFHo* where the number following the ‘s’ denotes progenitors with zero-age main sequence mass (Bizouard et al. 2021). The simulated waveforms are submerged by the aLIGO noise (Matthew et al. 2018), all two seconds long, pre-whitened, and sampled at 2^{14} Hz. We apply zero padding to the simulated waveforms that are under two seconds long. The original waveform is attenuated inversely proportional to the source distance. We consider twenty-one distances from 0.1 to 10 kpc with 0.5 kpc increment from 0.5 kpc, i.e., $\{0.1, 0.5, 1.0, \dots, 10.0\}$. A single realization in the time domain is presented in Figure 2, accompanied by its time-frequency representation obtained using the STFT.

The signal is submerged in a random aLIGO noise realization generated from its power spectral density. This process is repeated 100 times for each waveform and distance. Part of the procedure is illustrated in Figure 3. The time-frequency transformation (either STFT or Q-transform) produces a magnitude response in the form of an image to the CNN input. This procedure results in a total of

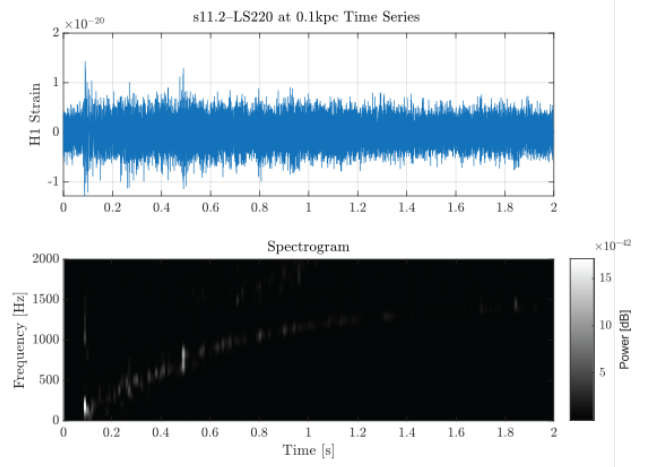


Figure 2. Top panel: CCSNe’s GW signature at 0.1 kpc embedded in the aLIGO noise. Bottom panel: The STFT spectrogram of the GW signal.

Table 1. Train, validation, and test split of the data. The same number of 2,100 instances of aLIGO noise was also included for each EOS model.

EOS	LS220					GShen	SFHo	
	s11.2	s15	s20	s25	s40	s15	s15	s20
Train	2,100	2,100	2,100	2,100	2,100	–	–	–
Validation	–	–	–	–	–	2,100	–	–
Test	–	–	–	–	–	–	2,100	2,100

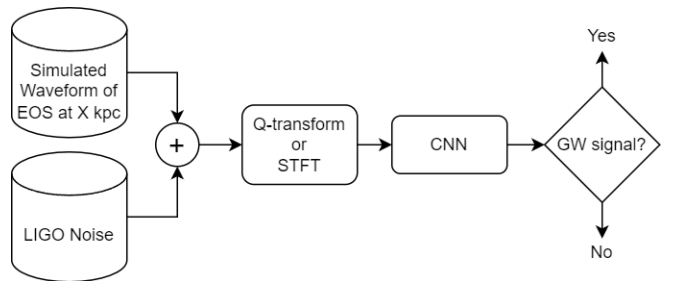


Figure 3. Data generation and analysis process. The noise data is generated by omitting the inclusion of the simulated waveform.

100 realizations \times 8 models \times 21 distances = 16,800 CCSNe signal observations. These observations are divided later into training, validation, and testing datasets. The split is as follows: 5 models for training, 1 for validation, and 2 for testing. See Table 1 for more details.

The negative class, i.e., aLIGO noise without any GW signals, is generated using the aLIGO power spectral density (Aasi et al. 2015). The same number of 16,800 noise realizations was generated to balance positive and negative classes.

The SNR across distances varies for the 8 EOS models, resulting in different degrees of difficulty for detection. To illustrate this, the SNR of two GW signals against the source distance is plotted in Figure 4. The initial SNR for *s15-SFHo* and *s20-SFHo* is 39.6 and 21.7 at 0.1 kpc, and the SNR at 10 kpc is 0.396 and 0.217, respectively. Their SNR profiles entail a more challenging signal detection task because when compared to a similar study in Astone et al. (2018),

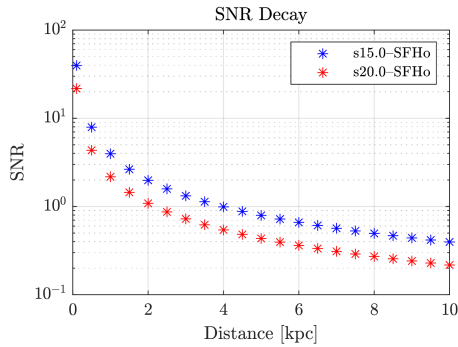


Figure 4. SNR of two signals across distances (0.1–10 kpc). These 2 signals are used as the test set.

their smallest SNR is 8, while our SNR drops below 1 when the source distance is beyond 4 and 2 kpc for *s15-SFHo* and *s20-SFHo*, respectively. Signals from these two EOS models are later used as the test set in the performance measurement of the trained deep convolutional neural network for CCSNe signal detection.

3.2 Data Processing

In this study, we use the STFT and QT to produce the spectrograms. The STFT is widely used in time-frequency analyses. We refer the reader to the extensive literature for its details and instead we focus on describing the QT. The QT has become an essential component in the aLIGO pipeline for searching gravitational wave bursts (Chatterji et al. 2004). Initially, it was applied in the field of music signal processing to differentiate similar notes played simultaneously (Brown 1991). The QT is a time-frequency transform designed to represent how the frequencies of a signal vary over time. This transform employs Gaussian windowed sinusoids to analyze signals, balancing time and frequency resolution. Our study uses a discrete version of the QT (Chatterji et al. 2004), incorporating a Hanning window in the frequency domain. The "Q" in Q-transform refers to the Q factor, which measures the window's width relative to its center frequency, enabling fine-tuning of the resolution. A high Q-factor indicates a narrow window in the time domain and a broader window in the frequency domain.

The time-series signal from aLIGO, denoted as $x(t)$, is projected onto $w(t - \tau, f)$ windowed complex sinusoids of frequency f centered around time τ , expressed mathematically (Chatterji et al. 2004) as

$$x(\tau, f) = \int_{-\infty}^{+\infty} x(t)w(t - \tau, f)e^{-i2\pi ft} dt. \quad (1)$$

For computational efficiency, the QT can alternatively be represented using the Fourier transform of the data time-series as

$$x(\tau, f) = \int_{-\infty}^{+\infty} \tilde{x}(\phi + f)\tilde{w}(\phi, f)e^{+i2\pi\phi\tau} d\phi, \quad (2)$$

with ϕ the frequency shift (Stockwell et al. 1996). This formulation allows the Fourier transform (FT) to be computed once. Subsequently, the Q-transform is calculated using this precomputed FT, applying a frequency shift and the window function in the frequency domain before inverting the FT. The QT used in our analysis is specifically adapted for aLIGO noise, normalizing the window to counteract the power spectral density of detector noise and accurately recovering the energy of transient bursts.

In this study, we utilize the QT implementation from the GWpy

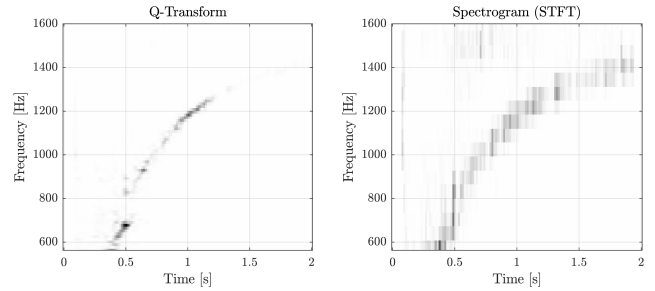


Figure 5. Comparison of QT and STFT spectrogram outputs of a simulated CCSNe event, for the same frequency range. The STFT spectrogram has been truncated for comparison purposes. Notice how the QT output has a higher resolution in both time and frequency axes.

Python package (Macleod et al. 2021) with specified parameters: *qrange* 100 to 200, *frange* 0 to 1600 Hz, *tres* 2/128 s, *fres* 1600/128 Hz, and *whiten* = False. The term *qrange* refers to the range of the Q-factor used in the QT and it is related to the time and frequency spread of the signal. A high Q-factor corresponds to a signal that is narrow in frequency but spread out in time, whereas a low Q-factor corresponds to a signal that is narrow in time but spread out in frequency. *frange* is the range of frequency to compute the QT. *tres* and *fres* are the time and frequency resolutions of the output spectrogram from QT, respectively, and they determine the size of the spectrogram. The remaining parameters are left at their default settings. The *frange* was selected based on the observation that all eight equations of state models studied exhibit frequency characteristics within this range. Prior to applying the QT, we band-pass the signal between 100 and 2000 Hz to attenuate irrelevant frequency components. This procedure is similarly applied to the noise input. It is important to note that this QT method interpolates the output to produce a high-resolution spectrogram on both time and frequency axes, allowing independent adjustments of *tres* and *fres*. Figure 5 demonstrates the superior time and frequency resolution of the QT compared to the spectrogram output from the short-time Fourier transform, particularly for the *s11.2-LS220* model at 0.1 kpc. The high-resolution images from the QT are directly used as inputs for the convolutional neural network, which is discussed in the following section.

3.3 Deep Convolutional Neural Network

Since our focus is on detecting the CCSNe GW events from the aLIGO interferometer by using the STFT and QT outputs, in 2 independent analyses, this is turned into an image classification problem. A similar work in Sassi et al. (2024) also used time-frequency spectrograms as input to classify human activity using CNN. We use transfer learning based on ResNet-18 (He et al. 2016) as the base network, leveraging its pre-trained parameters to alleviate training challenges and harnessing its capability to capture relevant lower-level features across domains. ResNet-18 is selected for its manageable complexity and the enhanced training efficiency afforded by its skip connections, which facilitate smoother gradient flows during backpropagation. Our network architecture, illustrated in Figure 6, processes input spectrograms resized to $224 \times 224 \times 3$ (width \times height \times channels). The configuration follows the original ResNet-18 design, incorporating a 2D convolutional layer with a 7×7 kernel, batch normalization (Ioffe & Szegedy 2015), and ReLU activation (Nair & Hinton 2010). However, the final fully-connected layer is modified to have 2 neurons corresponding to the two classes of interest: event signal and the aLIGO noise. We keep the *softmax* activation func-

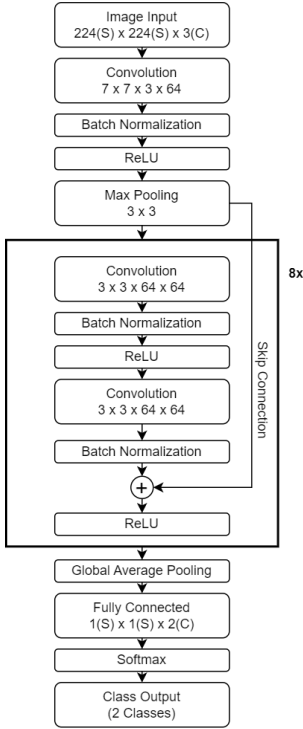


Figure 6. The architecture of the adapted deep convolutional neural network ResNet-18. The last fully connected layer is modified to suit the number of classes.

tion to output class probabilities for the positive and negative classes P_s and $P_n = 1 - P_s$, respectively, that sum up to one. In the last class output layer, the prediction is made based on the positive class threshold T , which is between 0 and 1. If $P_s \geq T$, then the class belongs to a signal; otherwise it belongs to the noise.

The dataset is divided into training, validation, and testing splits, as summarized in Table 1. Each entry in the table has 2,100 signal instances. The training and test split was performed to separate the EOSs, thus only the *LS220* was used for training, *GShen* for validation, and *SFH0* for testing. This ensures the CNN trained with one EOS is able to make detections with other EOSs. The same number of negative class instances was generated, so the trained network is not biased towards either class. To simulate the timing uncertainty inherent in actual detection scenarios and bolster the CNN’s robustness against overfitting, we employ random horizontal image translations up to 50% of the image width, as part of our data augmentation and neural network regularization strategy. The spectrogram h is rescaled to the range between 0 and 255 as

$$h_{\text{rescale}} = 255 \times \frac{h - \min(h)}{\max(h) - \min(h)}. \quad (3)$$

The rescaled spectrogram is then treated as a single channel gray scale image input to the CNN.

For training, we employ the Adam optimizer (Kingma & Ba 2017) with a learning rate of 10^{-6} , applied over 10 epochs, and include L_2 regularization set at 0.05. The network, which trains mini-batches of 128 training samples, does not freeze any layers, allowing all layers to update during training. These hyper-parameters were tuned such that small and similar training and validation losses were obtained. This setup achieved a final validation accuracy of 97.95%, which is very close to the final training accuracy. This indicates a successful optimization and learning generalization. Training progress, repre-

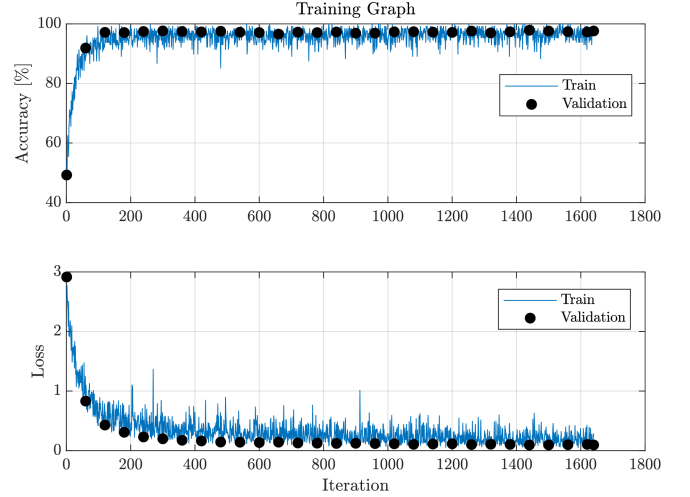


Figure 7. Accuracy and loss plot of the training process of QT-CNN, with validation data *s15-GShen*.

sented in Figure 7, plots classification accuracy and network loss over training iterations. The training converges in 400 iterations. We utilize weighted binary cross-entropy loss to penalize false negatives more heavily, enhancing the network’s sensitivity to genuine GW signals. This is given by

$$\text{Loss} = -\frac{1}{N} \sum_{i=1}^N (w_p \cdot y_i \cdot \log(P_{s,i}) + w_n \cdot (1 - y_i) \cdot \log(1 - P_{s,i})), \quad (4)$$

where $w_p = 5$ and $w_n = 1$ represent the weights for positive and negative class errors, respectively, with N the mini-batch size at 128, y_i the binary indicator of whether the signal instance is positive (1 for CCSNe signal) or not (0 for aLIGO noise). The ratio of weights w_p to w_n indicates that we are penalizing false negative classifications more, where a true CCSNe signal is misclassified as aLIGO noise.

For the CNN trained using the spectrograms produced by QT, which we call QT-CNN, the positive class threshold T is computed by maximizing the difference between true positive rate (TPR) and false alarm rate (FAR), which means maximizing the TPR and minimizing the FAR. The relationship is plotted in the left of Figure 9, and it indicates that when $P_s \geq 0.4$, the input is classified as a CCSNe signal. Therefore, for the QT-CNN, the threshold is $T = 0.4$. The classification threshold for the CNN trained using spectrograms produced by STFT, which we call STFT-CNN, is set by default at $T = 0.5$.

After hyper-parameters tuning, the network was trained again with training and validation data combined. The classification results from the test set are presented and discussed in the following section.

4 RESULTS AND DISCUSSION

The output spectrograms from QT and STFT have been used as the inputs to train the CNNs. We denote the CNNs as QT-CNN and STFT-CNN, respectively. The training procedures are the same for both models. TPR is first tested to get a quick overview of the model’s ability to classify the signal correctly. It is plotted in Figure 8 for the two signals in the test set: *s15.0-SFH0* and *s20.0-SFH0*. It

is expressed as the percentage of correct signal classifications over the total number of signal instances at a particular distance. In the QT-CNN case, for *s15.0-SFHo*, all signals are correctly predicted up to 10 kpc, where the SNR is just below 0.5. A steady, high true positive rate is observed for *s20.0-SFHo* at an SNR greater than 0.5, where the distance is 4 kpc. Beyond this SNR, the performance starts to drop as expected, which is not surprising considering the SNR at 10 kpc is just above 0.2. It can be observed that regardless of the EOS, the network is capable of correctly identifying the event signal at a high success rate for an SNR as low as 0.5. When comparing our result to that of [Astone et al. \(2018\)](#), we achieved a TPR of 100% for an SNR as low as 0.5 from the *s15.0-SFHo* model where they also achieved the same TPR but at an SNR of 20 (interpolated from Fig. 3a). In the STFT-CNN case, the CNN performs equally well for the *s15.0-SFHo* model but outperforms QT-CNN slightly for the *s20.0-SFHo* model at low SNRs, and achieves a TPR just above 20% for an SNR of approximately 0.2.

To further analyze the network’s confidence in classifying these two classes, a histogram of all positive class probabilities P_s is shown on the right of Figure 9. The histogram indicates a clear separation of the classes, with most instances of each class distributed at opposite ends of the histogram. This observation is in agreement with the insensitivity of the change in T to TPR – FAR around the middle plateau, suggesting a stable binary classification model. However, it is worth noting that there are a number of false negative samples at $P_s \leq 0.1$ consisting mostly of signals from beyond 6 kpc in the *s20.0-SFHo* model. A bar graph of their relative occurrence is plotted in Figure 10, confirming the expected behavior: as the distance increases, the SNR decreases inversely proportionally, causing the detection rate to drop.

The overall test set performance for all source distances is summarized in the confusion chart presented in Table 2. The values are expressed as percentages of the ground truth. We used the following metrics to evaluate the performance of the CCSNe GW signal classifier:

$$\text{True Positive Rate (TPR)} = \frac{\text{TP}}{\text{TP} + \text{FN}}, \quad (5a)$$

$$\text{False Alarm Rate (FAR)} = \frac{\text{FP}}{\text{FP} + \text{TN}}, \quad (5b)$$

$$\text{Precision} = \frac{\text{TP}}{\text{TP} + \text{FP}}, \quad (5c)$$

$$F_1 \text{ score} = 2 \times \frac{\text{precision} \times \text{TPR}}{\text{precision} + \text{TPR}}. \quad (5d)$$

For more information about these metrics, see, for example, [Fawcett \(2006\)](#). A TPR of 82.9% and 91.5% were achieved for QT-CNN and STFT-CNN, respectively, over an SNR range from 39.6 to 0.2. For the QT-CNN, out of 4,200 aLIGO noise and true event signal instances, 4,092 were correctly rejected as noise, and 3,482 we correctly identified as true event signals. This is equivalent to an overall true negative rate of 97.4%, a TPR of 82.90%, a FAR of 2.6%, a precision of 0.970, and a F_1 -score of 0.893. The TPR of 82.90% is higher than the 69% obtained in [Nunes et al. \(2024\)](#), despite our much lower SNR of 0.1 at 10 kpc, compared to their SNR of 20.

For the STFT-CNN, the TPR of 91.5% outperforms that of the QT-CNN, mainly due to the difficult instances of signals at very low SNR. It also gives a higher precision of 0.977, and a higher F_1 -score of 0.945. This might reflect how using a single Q-range limits the frequency bandwidth of the input data, and how a fixed Q-range might not be optimal for all EOSs. On the one hand, the STFT spectrogram data contain the full frequency bandwidth of CCSNe signal. On the other hand, the QT-CNN is penalized when using a single Q-range for all the EOSs, which limits the frequency

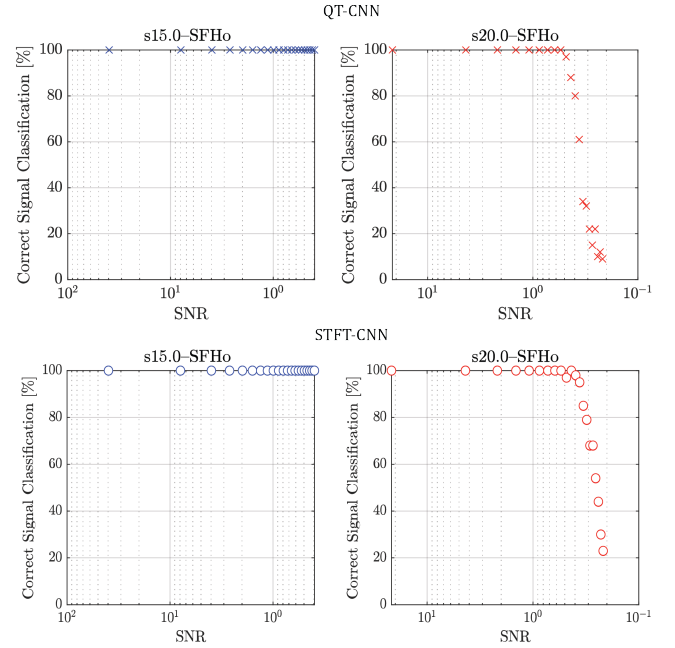


Figure 8. Top: True positive rate for *s15.0-SFHo* and *s20.0-SFHo* against SNR by using the QT as the input to the CNN. There are 2100 test images for each EOS model, positive class threshold $T = 0.4$. Bottom: True positive rate by using the STFT spectrogram as the input, positive class threshold $T = 0.5$.

Table 2. Confusion chart of the test set, positive class threshold $T = 0.4$ for QT-CNN and $T = 0.5$ for STFT-CNN. The percentages show the proportion of positive/negative detections relative to the ground truth. The lowest SNR in the test set is 0.2 from *s20.0-SFHo* at 10 kpc, as can be seen in Figure 4.

		Prediction			
		QT-CNN		STFT-CNN	
		aLIGO Noise	Event Signal	aLIGO Noise	Event Signal
Truth	aLIGO Noise	97.4 %	2.6 %	97.8 %	2.2 %
	Event Signal	17.1 %	82.9 %	8.5 %	91.5 %

bandwidth and excludes a significant portion of the low and high frequencies of the CCSNe signal. Given the current experimentation setup, STFT-CNN performs better than QT-CNN by detecting 8.6% more event signals, using the default class threshold of $T = 0.5$. Most of the 8.6% signals lie below $\text{SNR} = 0.5$ as shown in Figure 8.

To better understand the network’s decision process and ensure the classification made is justifiable, we examine the network with the Grad-CAM visualization ([Selvaraju et al. 2017](#)) for one realization from the predictions of both networks, shown in Figures 11 and 12. This method gives an idea of which parts of the input image are most relevant to a prediction. It reveals that the QT-CNN focuses correctly at a blob centering around 0.6 second and 800 Hz, where the signal’s time-frequency signature is most likely to appear. Similar results are obtained for the STFT-CNN, where the lower left region of the input contributes the most to the prediction of the signal class. However, note that the area above 1600 Hz is relevant for the prediction, a region that was omitted in the QT-CNN and could explain the difference in their performance.

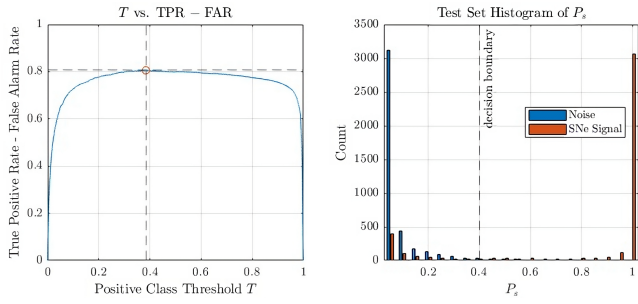


Figure 9. Left: Line plot of positive class threshold T against TPR – FAR for the QT-CNN case. The red marker at $T \approx 0.4$ denotes value of T that maximizes TPR while minimizes FAR. Right: Histogram of P_s for all test set images.

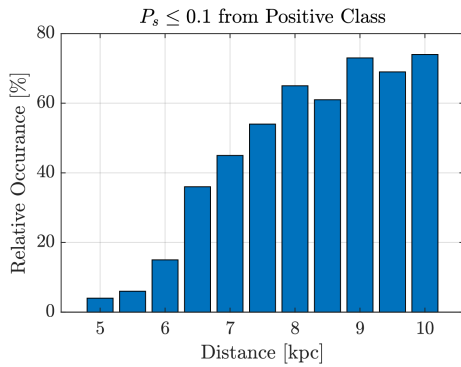


Figure 10. Relative occurrence of test samples from QT-CNN whose $P_s \leq 0.1$ from the *s20.0-SFHo* model.

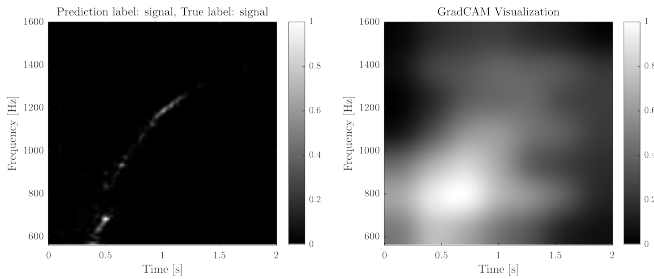


Figure 11. Left: QT spectrogram for a signal observation. Right: Grad-CAM visualization for the signal class prediction from the QT-CNN. The network focuses primarily on the region where the signal signature is most prominent.

5 CONCLUSIONS

Detecting GWs from CCSNe could be the next breakthrough for ground-based detectors, underscoring the critical importance of advancing detection techniques. In this paper, we have shown that a CNN can effectively detect these GW signals in the time-frequency domain. We investigated two pre-processing methods for the time-frequency domain analysis to train the CNNs: STFT and the QT. Both approaches, QT-CNN and STFT-CNN, perform similarly in terms of noise and signal identification down to an SNR of 0.5 in our test set. However, STFT-CNN outperforms QT-CNN in detecting signals below an SNR of 0.5. The TPRs are 0.83 and 0.92 for the QT-CNN and STFT-CNN for an SNR as low as 0.2, respectively. STFT-CNN

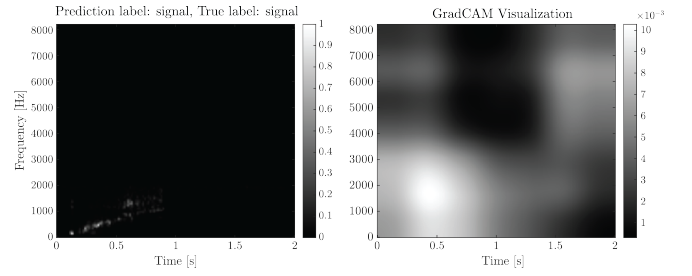


Figure 12. Left: STFT spectrogram for a signal observation. Right: Grad-CAM visualization for the signal class prediction from the STFT-CNN. The network concentrates most around the signal signature at 0.5 s and 1500 Hz.

also achieved a higher precision of 0.977, and a higher F_1 -score of 0.945.

Although STFT-CNN yielded better results for faint signals (those at extreme low SNRs), the experiment setup was designed for a singular CNN architecture to test both methods. This setup resulted in using one fixed Q-range to produce one QT spectrogram for each different data, which focuses on signal features in one portion of the whole frequency band. The choice of multiple Q-ranges to process each data will help cover the entire CCSNe signal features and the whole frequency band. Therefore, a CNN architecture adapted for multiple QT spectrograms for each signal could potentially improve the CNNs performance in detecting GWs from CCSNe.

Our experiment was conducted using only simulated CCSNe GW and aLIGO noise signals. The performance of our CNNs in the context of real signals and real noise remains uncertain at this stage, partly because a CCSNe GW signal has not yet been observed. This represents a limitation of the study and an area for future work. However, it should be noted that using aLIGO real noise data as pure noise for this analysis cannot be guaranteed due to various sources (e.g., environmental and instrumental factors), which could potentially introduce bias into the analysis, but may also reflect real-world complexities. Instead, a realistic aLIGO PSD (Matthew et al. 2018) was used for this analysis, based on extensive observational data and modeling of noise sources in the aLIGO interferometers. Considering datasets from real aLIGO noise to test our proposed CNNs is part of our planned future work.

Our CNNs, like other similar algorithms, lack interpretability. To address this, we used Grad-CAM visualization to highlight the relevance of spectrogram regions in the prediction process, although the exact decision-making remains unclear. Nevertheless, CNNs are well-suited when prediction is the primary focus of the analysis. In particular, they are especially useful for CCSNe detection, as they do not require a theoretical background for training.

We have demonstrated that CNNs trained in the time-frequency domain are viable methods for CCSNe detection at low SNRs. Our findings highlight the potential for exploring new techniques. Recent advances in neural-networks-based classification techniques (e.g., Song et al. (2024a,b); Abdullahi et al. (2024a,b)) present diverse opportunities for improving CCSNe detection. Similarly, the development of 3D simulations for CCSNe GW signals (e.g., Choi et al. (2024)) will provide more datasets and enable the training of CNNs in more realistic scenarios, improving detection accuracy. Additionally, a fast emulator for CCSNe signals (Eccleston & Edwards 2024), based on a deep convolutional generative adversarial network, has recently been proposed and may prove useful in developing advanced detection methods. The incorporation of these new developments will play an integral role in future work.

ACKNOWLEDGMENTS

Authors' work was supported by the Collaborative International Interuniversity Research, Innovation, and Development program-CIIRID: Continuity, Second Contest, from Pontificia Universidad Católica de Valparaíso, Chile, and Auckland University of Technology, New Zealand. PMR gratefully acknowledges support by the Marsden Fund Council grant MFP-UOA2131 from New Zealand Government funding, managed by the Royal Society Te Apārangi.

REFERENCES

- Aasi J., et al., 2015, *Classical and Quantum Gravity*, 32, 074001
- Abbott B., Jawahar S., Lockerbie N., Tokmakov K., 2016a, *Physical Review D*, 94, 064035
- Abbott B. P., et al., 2016b, *Physical Review Letters*, 116, 131103
- Abbott B. P., et al., 2017a, *Physical Review Letters*, 119, 161101
- Abbott B. P., et al., 2017b, *The Astrophysical Journal Letters*, 848, L13
- Abdullahi S. B., Chamnongthai K., Gabralla L. A., Chiroma H., 2024a, *IEEE Sensors Journal*, 24, 37630
- Abdullahi S. B., Chamnongthai K., Bolon-Canedo V., Cancela B., 2024b, *Expert Systems with Applications*, 248, 123258
- Agazie G., et al., 2023, *The Astrophysical Journal Letters*, 951, L8
- Antelis J. M., Cavaglia M., Hansen T., Morales M. D., Moreno C., Mukherjee S., Szczepańczyk M. J., Zanolin M., 2022, *Physical Review D*, 105, 084054
- Astone P., Cerdá-Durán P., Di Palma I., Drago M., Muciaccia F., Palomba C., Ricci F., 2018, *Physical Review D*, 98, 122002
- Bizouard M.-A., Maturana-Russel P., Torres-Forné A., Obergaulinger M., Cerdá-Durán P., Christensen N., Font J. A., Meyer R., 2021, *Physical Review D*, 103, 063006
- Brown J. C., 1991, *The Journal of the Acoustical Society of America*, 89, 425
- Chan M. L., Heng I. S., Messenger C., 2016, *Physical Review D*, 94, 064035
- Chatterji S., Blackburn L., Martin G., Katsavounidis E., 2004, *Classical and Quantum Gravity*, 21, S1809
- Choi L., Burrows A., Vartanyan D., 2024, Gravitational-Wave and Gravitational-Wave Memory Signatures of Core-Collapse Supernovae ([arXiv:2408.01525](https://arxiv.org/abs/2408.01525)), <https://arxiv.org/abs/2408.01525>
- Danzmann K., Rüdiger A., 2003, *Classical and Quantum Gravity*, 20, S1
- Eccleston T., Edwards M. C., 2024, *Physical Review D*, 110, 104055
- Einstein A., et al., 1916, *Annalen der Physik*, 49, 769
- Fawcett T., 2006, *Pattern Recognition Letters*, 27, 861
- He K., Zhang X., Ren S., Sun J., 2016, in 2016 IEEE Conference on Computer Vision and Pattern Recognition (CVPR). pp 770–778, [doi:10.1109/CVPR.2016.90](https://doi.org/10.1109/CVPR.2016.90)
- Ioffe S., Szegedy C., 2015, Batch Normalization: Accelerating Deep Network Training by Reducing Internal Covariate Shift ([arXiv:1502.03167](https://arxiv.org/abs/1502.03167))
- Kingma D. P., Ba J., 2017, Adam: A Method for Stochastic Optimization ([arXiv:1412.6980](https://arxiv.org/abs/1412.6980))
- Klimenko S., Yakushin I., Mercer A., Mitselmakher G., 2008, *Classical and Quantum Gravity*, 25, 114029
- Krishna B., Devi G. D., V S., J M., 2023, in 2023 International Conference on System, Computation, Automation and Networking (ICSCAN). pp 1–6, [doi:10.1109/ICSCAN58655.2023.10395616](https://doi.org/10.1109/ICSCAN58655.2023.10395616)
- Macleod D. M., Areeda J. S., Coughlin S. B., Massinger T. J., Urban A. L., 2021, *SoftwareX*, 13, 100657
- Matthew E., Riccardo S., Salvatore V., Evan H., 2018, *LIGO-T1500293-v13*
- Müller B., Janka H.-T., Marek A., 2013, *The Astrophysical Journal*, 766, 43
- Nair V., Hinton G. E., 2010, in Proceedings of the 27th International Conference on International Conference on Machine Learning. ICML'10. Omnipress, Madison, WI, USA, pp 807–814
- Nunes S., Escrig G., Freitas O. G., Font J. A., Fernandes T., Onofre A., Torres-Forné A., 2024, Deep-Learning Classification and Parameter Inference of Rotational Core-Collapse Supernovae ([arXiv:2403.04938](https://arxiv.org/abs/2403.04938))
- Sassi M., Haleem M. S., Pecchia L., 2024, Spectrogram-Based Approach with Convolutional Neural Network for Human Activity Classification. Springer Nature Switzerland, pp 387–401, [doi:10.1007/978-3-031-49068-2_40](https://doi.org/10.1007/978-3-031-49068-2_40)
- Selvaraju R. R., Cogswell M., Das A., Vedantam R., Parikh D., Batra D., 2017, in 2017 IEEE International Conference on Computer Vision (ICCV). pp 618–626, [doi:10.1109/ICCV.2017.74](https://doi.org/10.1109/ICCV.2017.74)
- Song X., Wu C., Song S., Stojanovic V., Tejado I., 2024a, *Engineering Applications of Artificial Intelligence*, 131, 107832
- Song X., Peng Z., Song S., Stojanovic V., 2024b, *Communications in Non-linear Science and Numerical Simulation*, 132, 107945
- Stockwell R., Mansinha L., Lowe R., 1996, *IEEE Transactions on Signal Processing*, 44, 998
- Vartanyan D., Burrows A., Wang T., Coleman M. S. B., White C. J., 2023, *Phys. Rev. D*, 107, 103015
- Vink J., 11 November 2020, Physics and Evolution of Supernova Remnants. Springer Cham, [doi:10.1007/978-3-030-55231-2](https://doi.org/10.1007/978-3-030-55231-2)
- Wang R., Zhuang Z., Tao H., Paszke W., Stojanovic V., 2023, *ISA Transactions*, 142, 123
- Wolfe N. E., Fröhlich C., Miller J. M., Torres-Forné A., Cerdá-Durán P., 2023, *The Astrophysical Journal*, 954, 161

This paper has been typeset from a $\text{\TeX}/\text{\LaTeX}$ file prepared by the author.